A New Satellite-Based Indicator for Estimation of the Western North Pacific Tropical Cyclone Current Intensity

Xiao-Yong Zhuge, Jian Guan, Fan Yu, and Yuan Wang

***Abstract*—A technique to estimate tropical cyclone (TC) current intensity based on geostationary satellite infrared window (IRW) and water vapor (WV) imagery is explored in this paper. First, to combine the advantages of the IRW imagery and the WV minus IRW (WV-IRW) imagery, a WV-IRW-to-IRW ratio (WIRa)-based indicator is proposed. This indicator not only can display the inner-core convection's symmetrization level and vigor but also is able to screen out thin cirrus, stratospheric WV anomaly, and overshooting tops from average deep convection. It is highly correlated with the best track minimum sea-level pressure and thus used to estimate the western North Pacific TC current intensity. Detailed analyses have demonstrated that the WIRa-based indicator can further improve the estimation of TC current intensity alongside the existing algorithms. The WIRa-based indicator is designed based on the hypothesis that "overshooting top is more useful for forecasting than initial estimation," and the satisfying results of the WIRa-based method perhaps provide indirect evidence to support this hypothesis in turn.**

***Index Terms*—Meteorology, remote sensing, satellite applications, tropical cyclone.**

I. Introduction

WESTERN North Pacific (WNP) tropical cyclones (TCs) are the most devastating natural disasters over East and Southeast Asia, causing catastrophic damage to coastlines and several hundred miles inland. Real-time monitoring of a TC's generation, movement, and intensification will ensure timely preparedness and response to the TC impact and will efficiently reduce the economic loss and personnel casualty. Geostationary meteorological satellite remote sensing has the advantages of higher temporal resolution compared with polar satellite microwave detecting [1]–[3] and wider observation range compared with aircraft reconnaissance [4]–[6]. It also covers ocean and sparsely populated areas where ground-based radars cannot cover sufficiently [7]–[10]. For these reasons, geostationary meteorological satellite remote sensing is regarded as the most widespread tool for estimating TC intensity over the WNP [11].

The history of monitoring TC intensity using satellite imageries can be traced back to the 1960s [12]–[14]. Dvorak summarized the previous research and proposed a systematic method by equating satellite cloud signatures to TC intensity. This method became known as Dvorak technique (DT) [15], [16]. DT's major shortcomings include its many subjective rules and its heavy reliance on the expertise levels of TC forecasters and satellite analysts. The digital Dvorak method [17], the objective DT (ODT) [18], and the subsequent advanced ODT (AODT) [19] gradually achieved a computer-driven automatization and lessened the uncertainty and variability of TC intensity estimation caused by the subjectivity of TC forecasters in the original DT. The advanced DT (ADT) [20], which is referred to as the latest version of the DT, proposed some additions and modifications to the AODT. All these five versions of DT methods, in general, estimate TC intensity based on the cloud pattern and feature recognition with visible/infrared imageries [11].

DT methods have been operationally employed at operational forecast centers (OFCs) around the world. However, various DT rules and constraints are derived or modified by the OFCs [11], which may result in a great divergence in the estimation of TC intensity even for the same TC. Nakazawa and Hoshino compared the tropical numbers (T#s) and current intensity number (CI#) in Japan Meteorological Agency (JMA) and the Joint Typhoon Warning Center (JTWC) data sets from 1987 to 2006 and found that the T# and CI# values estimated by JTWC were higher than those by JMA during the periods of 1992–1997 and 2002–2005, particularly for typhoon cases with rapid intensification before the mature stage and/or slow/delayed weakening after the mature stage [21]. The divergence in the estimation of typhoon intensity imposes the necessity to define more practical, unambiguous, and recognizable estimation indicators to advance the ability and improve the accuracy in estimating TC intensity.

Recently, some new TC intensity indicators have been developed by employing the geostationary satellite imagery. Chao *et al.* derived an indicator based on the rotation speed of

Manuscript received October 21, 2014; revised January 30, 2015 and March 16, 2015; accepted April 16, 2015. Date of publication May 20, 2015; date of current version June 10, 2015. The work of X.-Y. Zhuge and F. Yu was supported in part by the National Fundamental Research 973 Program of China under Grant 2013CB430100 and Grant 2015CB452800 and in part by the National Natural Science Foundation of China under Grant 41275030. X.-Y. Zhuge was also supported by the Scholarship Award for Excellent Doctoral Student granted by the Ministry of Education. Y. Wang was supported by the National Natural Science Foundation of China under Grant 41275057. *(Corresponding authors: Fan Yu and Yuan Wang.)*

X.-Y. Zhuge, F. Yu, and Y. Wang are with the School of Atmospheric Sciences and the Key Laboratory of Mesoscale Severe Weather of the Ministry of Education, Nanjing University, Nanjing 210093, China (e-mail: yufan@nju.edu.cn; yuanasm@nju.edu.cn).

J. Guan is with the Laboratory for Climate and Ocean-Atmosphere Studies, Department of Atmospheric and Oceanic Sciences, School of Physics, Peking University, Beijing 100871, China.

Color versions of one or more of the figures in this paper are available online at http://ieeexplore.ieee.org.

Digital Object Identifier 10.1109/TGRS.2015.2427035

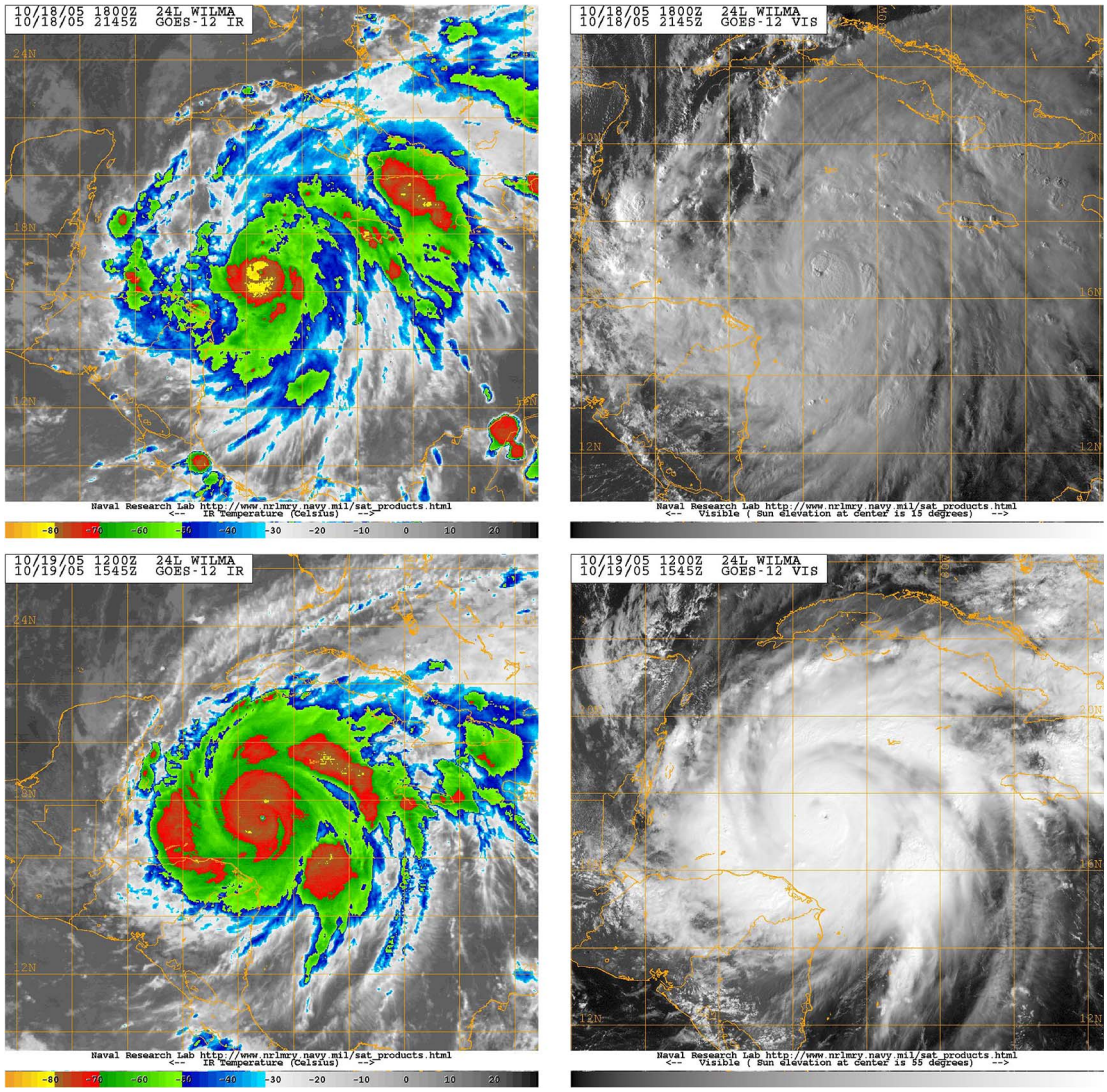

Fig. 1. (Left) IRW and (right) visible imagery of Hurricane Wilma (2005) around (top) 21:45 UTC on 18 October 2005 and (bottom) 15:45 UTC on 19 October 2005. The corresponding central pressures are 975 and 882 hPa, respectively. The imageries are all downloaded from http://www.nrlmry.navy.mil/TC.html.

the TC rainband [22]. Piñeros *et al.* developed a deviation-angle variance technique [23] that can quantify the symmetrization level of the infrared cloud signature, and Ritchie *et al.* provided its improved version [24]. Olander and Velden counted the pixels with positive differences between the water vapor (WV) channel brightness temperature Tb_{WV} and infrared window (IRW) channel brightness temperature Tb_{IRW} $(Tb_{\mathrm{WV-IRW}})$ [25]. They argued that positive $Tb_{\mathrm{WV-IRW}}$ indicates the presence of vigorous convection "overshooting" into the stratosphere, and this signal in the TC inner core can be used for TC future 12-h intensity estimation. Jaiswal *et al.* provided a historical imagery database that includes TC intensity and convective feature information extracted from hurricane satellite (HURSAT) data set to estimate current TC intensity based on the imagery matching approach [26].

Broadly speaking, there are two approaches for estimating TC intensity from geostationary satellite observations: 1) the convection's organization level; and 2) the convective vigor (e.g., the minimum Tb_{IRW} or the number of pixels with $Tb_{\mathrm{IRW}} < 200$ K) according to current literature works. However, one should be careful when using the second approach because the inner-core convective vigor is more useful for forecasting than initial estimation, as demonstrated by Olander and Velden [25]. If the positive relationship between convective vigor and TC current intensity is admitted unconditionally, this means that the cyclone should be intense enough when the convection's extreme case (i.e., the overshooting convection) is detected, which is at variance with the observations and model simulation results. A famous counterexample is the Atlantic Hurricane Wilma (2005). As shown in Fig. 1, a near-center overshooting top with Tb_{IRW} near 180 K was detected at 21:45 UTC on 18 October when its central pressure is 975 hPa, but the overshooting top disappeared and Tb_{IRW} increased to 190 K at 15:45 UTC on 19 October when its central pressure reached 882 hPa. In addition, Rozoff *et al.* [27] and Wang [28] argued that the rapid filamentation zone of an intense TC would highly distort and even suppress the intense convection. Zhuge *et al.* [under review] have demonstrated that less than 25% of the TCs above Category 4 in the Saffir–Simpson scale are found with the inner-core overshooting convection (the climatological average is approximately 35%) according to the Tropical Rainfall Measuring Mission satellite observations. Therefore, overshooting

top may be not suitable to serve as an indicator of TC current intensity.

In this paper, we conducted an estimation experiment of TC current intensity based on the aforementioned hypothesis and finally proposed a new indicator for the estimation of the WNP TC current intensity. The remaining part of this paper is organized as follows. Section II describes the data and preprocess. The new indicator is proposed in Section III, and its feasibility is discussed in Section IV. The method of estimating TC intensity over the WNP is tested and verified in Section V. Discussion and conclusions are given in Section VI. To help explain the functions of the new indicator, the sensitivity of IRW and WV-IRW to the cloud and atmospheric parameters is analyzed based on radiative transfer model results in the Appendix.

II. Data and Preprocess

The region of interest (ROI) covers the WNP Basin from 10° to 45° N and from 100° to 150° E. The time period for this study is from 2006 to 2011 and covered by two Japanese geostationary satellites, i.e., Multifunctional Transport Satellite (MTSAT)-1R and MTSAT-2. Hourly or half-hourly satellite data are obtained from the National Satellite Meteorological Center of China Meteorological Administration (via http://satellite.cma.gov.cn/PortalSite/Data/Satellite.aspx) and remapped to an equal longitude–latitude grid with a resolution of 0.05°. Both MTSAT-1R and MTSAT-2 have five spectral channels, among which IRW channel (10.3–11.3 μm) and WV channel (6.5–7.0 μm) are selected for this study.

The validation data set should be determined before the estimate equation is established. The aircraft reconnaissance obviously provides the most accurate observations [11]. Although the global aircraft reconnaissance program has been deactivated since 1987 except for the Atlantic Basin to the west of 55° W [29], a few dropsondes were launched from aircraft reconnaissance flights during special observation campaigns, e.g., The Observing System Research and Predictability Experiment (THORPEX) Pacific Asian Regional Campaign (TPARC)/the Tropical Cyclone Structure (TCS)-08 program in 2008 and the Impact of Typhoons on the Ocean in the Pacific (ITOP)/TCS-10 program in 2010 (http://www.aoml.noaa.gov/hrd/data_sub/hurr.html). There are an insufficient number of TC cases for statistically significant validation of the method using dropsondes alone; therefore, they cannot be utilized as validation data for this study. JMA best track (BT) data sets [30] (via http://www.jma.go.jp/jma/jma-eng/jma-center/rsmc-hp-pub-eg/besttrack.html) are ultimately chosen as validation data for this study. The BT intensities are initially calculated by DT methods and then modified by other observations such as station and ship weather reports, aircraft reconnaissance, and Doppler radar. Thus, BT intensities are the data closest to the truths at present.

This paper only focuses on TC cases with 10-min average maximum sustainable wind (MSW) above 85 knots at the peak intensity. However, the entire life cycle of every single TC case is examined, and thus, the results are applicable to other TC cases. There are 42 TCs in total over the WNP reaching this level during the study period. However, only 35 cases are selected into the database used for this study (see Fig. 2). The other seven cases are removed because of the following reasons.

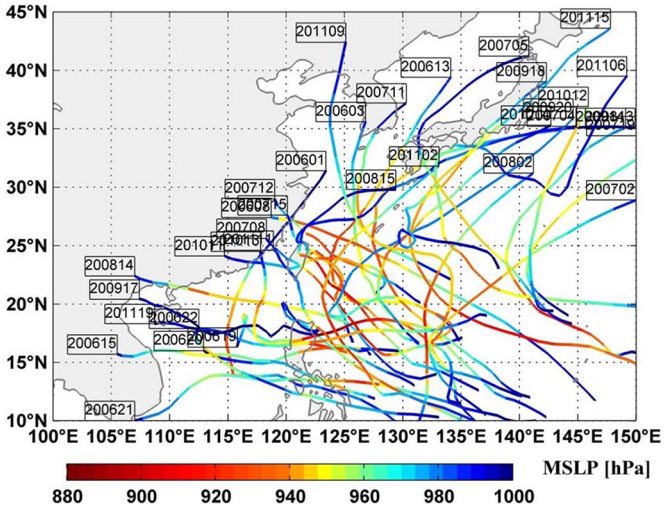

Fig. 2. ROI and TC database used in this paper.

1) Satellite data are missing during the time periods from March 13 to 24, 2008, and from May 29 to September 11, 2008. Nakri (200805) and Fengshen (200806) were within this period and thus removed. The first half of life history of Sinlaku (200813) was also affected, but this case is still retained in the database.
2) The scan lines near the TC center were often mutilated during the lifetime of Nida (200922) and Kujira (200901).
3) The majority of the trajectory was out of the ROI [i.e., Ioke (200612), Yagi (200614), and Vamco (200910)].

TC intensities are sensitive to the dynamic and thermodynamic processes within the inner-core region [31], [32]. As a consequence, the IRW and WV information within a 1.5° (approximate 150 km) radius from the TC center is extracted in advance. The TC center location is initially determined by the interpolated JMA BT data. Similar to Olander and Velden [25], it would be manually adjusted when the IRW or WV-IRW imagery suggests that the center should be moved. The center is almost always adjusted in TCs with well-defined eyes; in tropical storms, the center is only moved if there is convincing evidence to relocate it. Moreover, the radius of 150 km is an empirical parameter for average TC inner-core size [33]. Note that Olander and Velden [25] used 1.25° (approximately 136 km) as the outermost radius of the inner-core region on the infrared imagery, and Chao *et al.* [22] used 130 km, which is close to the size used in this paper.

In addition, note that we choose minimum sea-level pressure (MSLP) rather than MSW as the measure of TC intensity mainly because different average time periods are used in MSW calculation. JMA's wind is 10-min averaged, JTWC's wind is 1-min averaged, and the dropsonde wind is instantaneous. Therefore, winds from these three products cannot be compared directly [34], although the empirical relationships between 10-min average wind speed and 1-min average wind speed have been set up [35]–[37]. In addition, the asymmetric wind structures in the storm can also cause deviations from the actual intensity [20].

TABLE I
EFFECTS OF CONVECTION, WV ANOMALY, AND CIRRUS ON Tb_{IRW} AND $Tb_{\mathrm{WV-IRW}}$

		Tb_{WV-IRW}		
		Negative	Weakly positive (e.g., 0-1.5K)	Positive (e.g., 3K)
Tb_{IRW}	Very low (e.g., 190K)		Overshooting top / thin cirrus near the tropopause	Overshooting top and/or Stratospheric WV anomaly
	Low (e.g., 205K)	thin cirrus	deep convection / thick cirrus	Stratospheric WV anomaly
	Median (e.g., 230K)	weak convection /cirrus		

III. DEFINITION OF THE NEW INDICATOR

According to the idealized experiment results with the radiative transfer model discussed in the Appendix and/or in other literature works, the effects of convection, WV anomaly, and cirrus on $Tb_{\mathrm{WV-IRW}}$ are qualitatively summarized in Table I. Negative $Tb_{\mathrm{WV-IRW}}$ is generated by cirrus and weak convection, whereas large positive $Tb_{\mathrm{WV-IRW}}$ is produced by stratospheric WV anomaly and overshooting top. The thin cirrus near the tropopause and overshooting top have a very low Tb_{IRW}. The average deep convection is often accompanied by a weakly positive $Tb_{\mathrm{WV-IRW}}$ and a Tb_{IRW} of near 205 K. However, limited by the authors' knowledge and the geostationary satellites' detection ability, currently, there are no approaches to distinguish thick cirrus from deep convection. Note that the results here can be used in the qualitative analysis rather than quantitative analysis. In addition, it should be declared that we want to distinguish between the average deep convection and the overshooting convection, but this does not imply that we deny that overshooting convection is an extreme case of deep convection.

As aforementioned in the introduction section, the average deep convection is the useful information for the estimation of TC current intensity from the imagery of geostationary satellite, whereas the overshooting top and nonconvection are the disturbing factors. In the estimation, the first issue is to distinguish the average deep convection from the overshooting top and nonconvection. According to Table I, it is very convenient to distinguish the average deep convection from the weak convection, thin cirrus, and stratospheric WV anomaly by using $Tb_{\mathrm{WV-IRW}}$ and to distinguish the average deep convection from the overshooting top and cirrus near the tropopause by using Tb_{IRW}. Nevertheless, this paper will propose an indicator, which can combine the functions of Tb_{IRW} and $Tb_{\mathrm{WV-IRW}}$, simultaneously distinguishing the average deep convection from the thin cirrus, stratospheric WV anomaly, and overshooting top. The derivation of the new indicator involves four steps.

A. First Step: Screening Out the Weak Convection Pixels

A Tb_{IRW} threshold should be determined to exclude a majority of weak convection pixels. According to the frequency plot of inner-core Tb_{IRW} (see Fig. 3), about 40% of pixels are with Tb_{IRW} greater than 215 K. Therefore, the 215-K Tb_{IRW} is used as the benchmark index to screen out the weak convection pixels. This threshold was also utilized in [38]. Because of the strong correlation between $Tb_{\mathrm{WV-IRW}}$ and Tb_{IRW} [39], [40], the value of $Tb_{\mathrm{WV-IRW}}$ will be approximately higher than -5 K when $Tb_{\mathrm{IRW}} < 215$ K. Accordingly, the value of $Tb_{\mathrm{WV-IRW}}$ ranges from -5 K to 5 K and that of Tb_{IRW} ranges approximately from 185 K to 215 K for the remaining inner-core pixels.

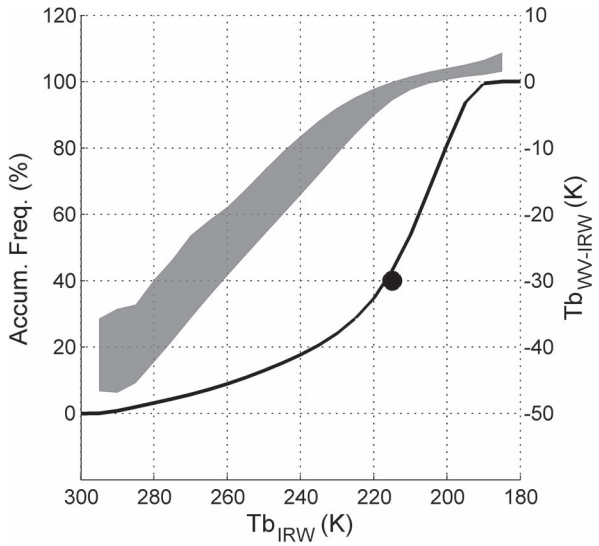

Fig. 3. (Solid line) Frequency of inner-core Tb_{IRW} less than brightness temperature values along the bottom x-axis scale and (gray shading) distribution of $Tb_{\mathrm{WV-IRW}}$ versus Tb_{IRW}. Circles represent criteria used in distinguishing the weak convection and deep convection apart.

B. Second Step: Calculating the WIRa

The WV-IRW-to-IRW ratio (WIRa) value for every pixel is calculated in each individual satellite image. The magnitude of Tb_{IRW} variation (10^1) is smaller than the magnitude of Tb_{IRW} itself (10^2). If Tb_{IRW} is directly used as the denominator, it only makes a tiny contribution to WIRa (given that Tb_{IRW} ranges from 185 K to 215 K, the relative variational amplitude of WIRa caused by Tb_{IRW} is at most $((1/185\ \mathrm{K}) - (1/215\ \mathrm{K})) \div (1/185\ \mathrm{K}) = 13.95\%$). Therefore, Tb_{IRW} minus a referenced temperature Tb_{ref} is used for WIRa, which is finally defined as

$$\mathrm{WIRa} = 100 \cdot \frac{Tb_{\mathrm{WV-IRW}}}{Tb_{\mathrm{IRW}} - Tb_{\mathrm{ref}}} \tag{1}$$

where the amplification factor 100 is added to raise the order of the magnitude of WIRa to 1 while it has no influence on WIRa's behaviors. Tb_{ref} is set to be 180 K to be smaller than the minimum Tb_{IRW}. At this time, the relative variational amplitude of WIRa due to Tb_{IRW} is at most $((1/(185\ \mathrm{K} - 180\ \mathrm{K})) - (1/(215\ \mathrm{K} - 180\ \mathrm{K}))) \div (1/(185\ \mathrm{K} - 180\ \mathrm{K})) = 85.71\%$. In this way, WIRa for stratospheric WV anomaly and overshooting top tends to have larger values (approximately 15–30), whereas WIRa for the thin cirrus and weak convection tends to have negative values, and thus, the average deep convection has a moderate value (approximately 0–15).

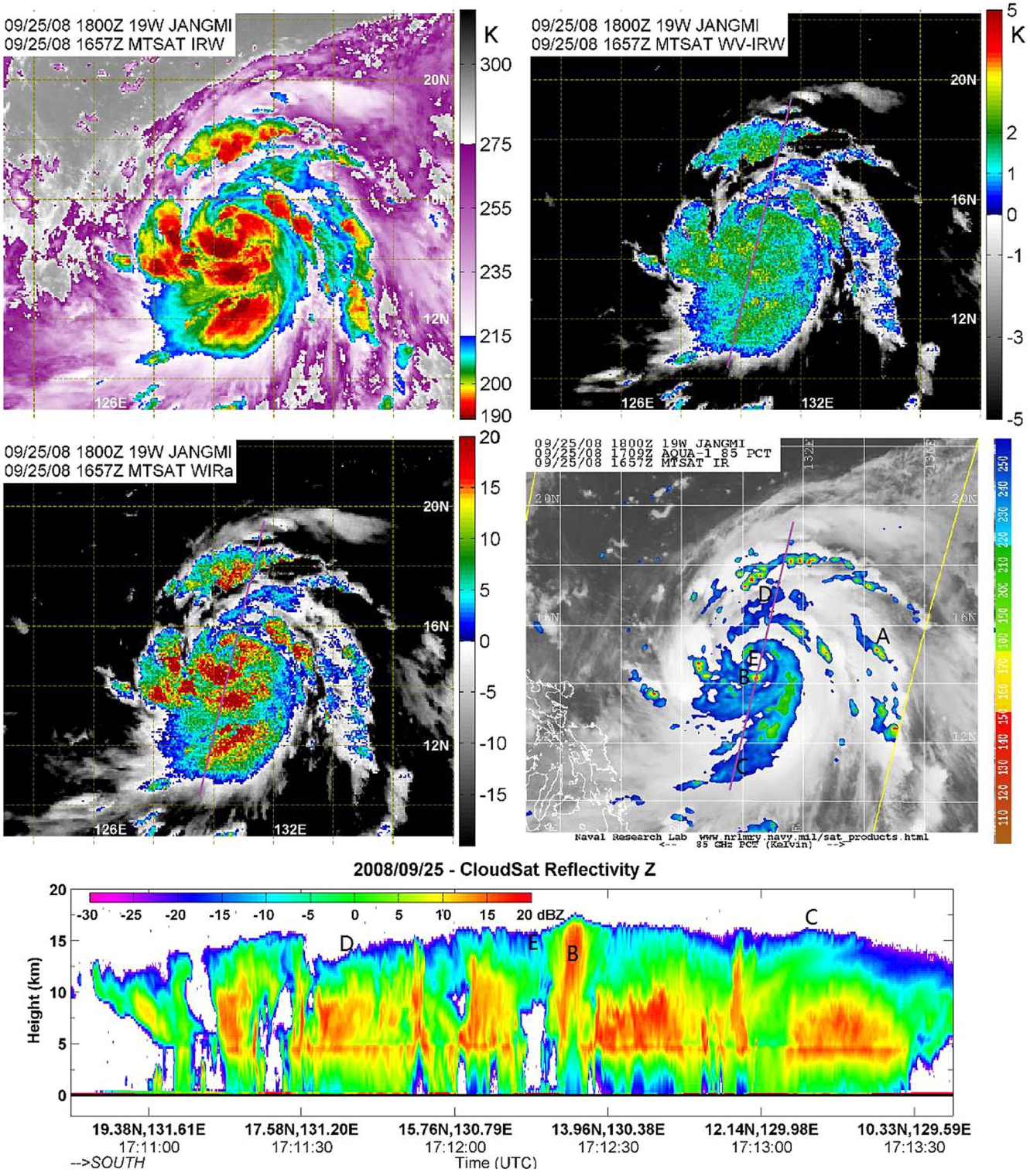

Fig. 4. Imagery of Jangmi (200815) around 17:00 UTC on 25 September 2008: (top left) MTSAT-1R IRW imagery, (top right) MTSAT-1R WV-IRW imagery, (center left) WIRa imagery, (center right) Aqua 85-GHz PCT passive microwave image, (purple line) CloudSat track, and (bottom) CloudSat reflectivity profiles along its track. Discussion on regions A–E is in the text.

The functions of WIRa are verified by the real case (see Fig. 4). The intensity of Jangmi (200815) at 17:00 UTC on 25 September 2008 is 965 hPa. According to CloudSat reflectivity vertical profile, regions C and D were both moderate convection. However, region C was covered by thick cirrus; thus, the Tb_{IRW} in region C was far below that that in region D, and $Tb_{\mathrm{WV-IRW}}$ was about 3.5 K. Accordingly, WIRa was about 4 for region D, whereas it was 35 for region C. According to an 85-GHz polarization corrected temperature (PCT) passive microwave image, regions A and B were both overshooting tops with Tb_{IRW} equal to 190 K, but $Tb_{\mathrm{WV-IRW}}$ was 3.5 K for region B whereas it was about 1 K for region A. This difference

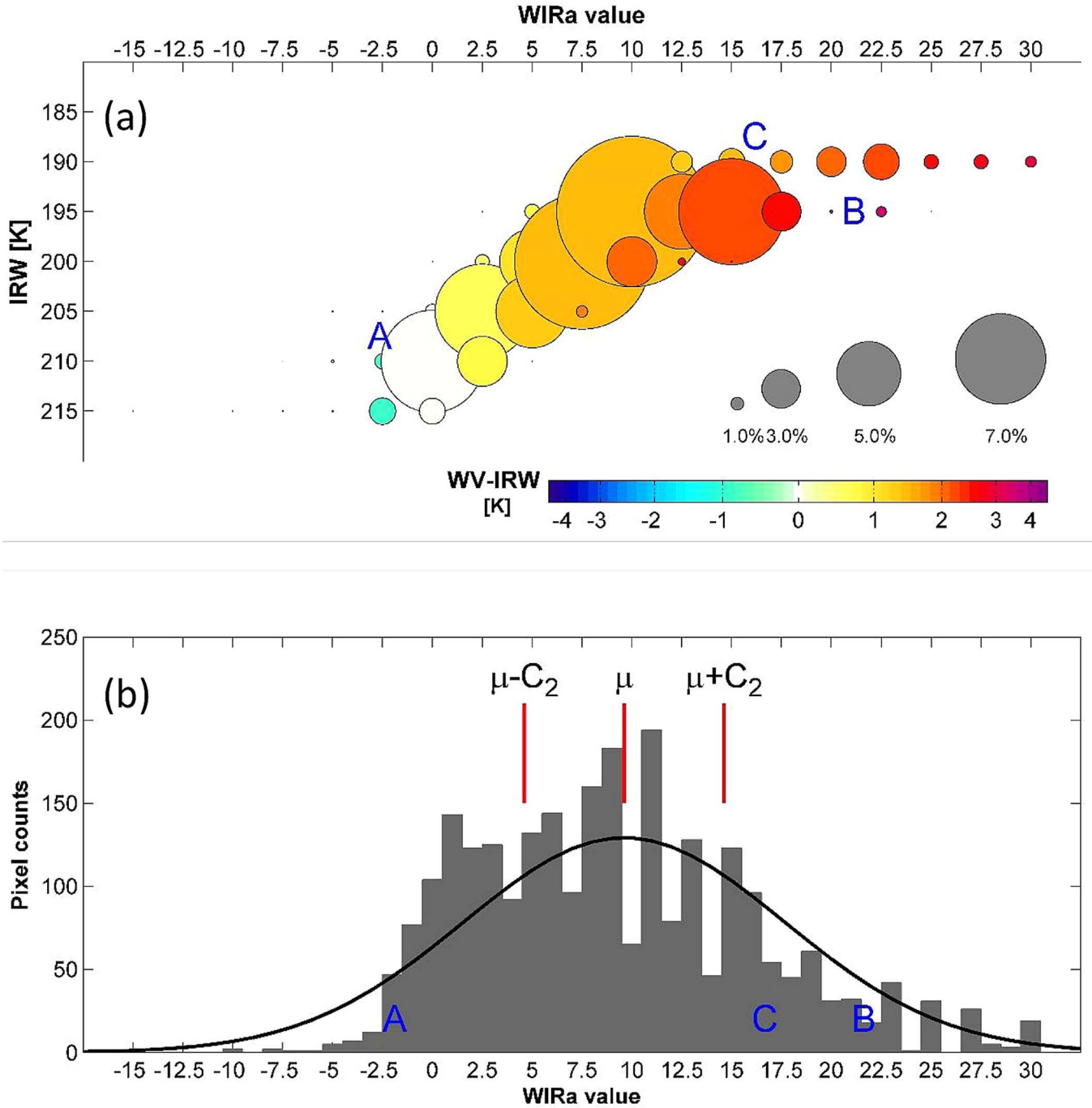

Fig. 5. Frequency distribution diagram for Tb_{IRW}, $Tb_{\mathrm{WV-IRW}}$, and WIRa. Larger cycle corresponds to a higher frequency. (b) (Gray bars) WIRa distribution, (black lines) normal distribution with the same mean value and standard deviation, along with the value of μ, $\mu - C_2$, and $\mu + C_2$ indicated as red vertical lines. All the brightness temperature information is from MTSAT-1R imagery of Jangmi (200815) around 17:00 UTC on 25 September 2008. The regions of thin cirrus (marked with A), overshooting top and stratospheric WV anomaly (marked with B), and cirrus near the tropopause (marked with C) are also shown.

may be associated with stratospheric WV anomaly (it is difficult to be verified because stratospheric WV anomaly cannot be directly detected with current spaceborne instruments). However, the WIRa values in these regions were all over 10. The eye region was covered by thick cirrus, and $Tb_{\mathrm{WV-IRW}}$ was weakly positive and thus cannot be distinguished from other convection. The outer-core region was wide-spreading thin cirrus, such that Tb_{IRW} was far above 215 K and WIRa was negative.

C. Third Step: Calculating the Mean WIRa Value

For all the inner-core pixels with $Tb_{\mathrm{IRW}} < 215$ K on a given image, the distribution of WIRa appears normal-like (see Fig. 5). Thin cirrus (marked with A) are distributed on the left, stratospheric WV anomaly and overshooting top (marked with B) and cirrus near the tropopause (marked with C) are generally on the right, and average deep convection is in the center. Relative to the cirrus and overshooting convection pixels, the average deep convection pixels are dominant, and

thus, the mean WIRa value μ is also the center position of WIRa distribution of average deep convection.

D. Last Step: Counting the Average Deep Convection

Back to Fig. 5(b), supposing that the average deep convection has a WIRa value within the range of $[\mu - C_2, \mu + C_2]$, we now count how many inner-core pixels have WIRa values within $[\mu, \mu + C_2]$ (hereafter, WIRa $[\mu, \mu + C_2]$). μ is set to be 0 when it is negative. Because the interference elements and average deep convection pixels are separate, the WIRa $[\mu, \mu + C_2]$ counts (it is also called "WIRa #" for short) reflect half of the amount of average deep convection pixels. A sensitivity test shows that the results of TC intensity estimation with parameter C_2 from 1 to 10 are scarcely discrepant (figure omitted), and thus, in this paper, C_2 is set to 5 subjectively.

It is also shown in Fig. 5(b) that the μ value is approximately 9 and $\mu + 5$ is approximately 14. However, the WIRa values of stratospheric WV anomaly and overshooting pixels range approximately from 15 to 30, and that of thin cirrus pixels is less than 0. This means that the pixels of thin cirrus, stratospheric WV anomaly, and overshooting tops would not be counted into the WIRa #. Therefore, WIRa # excludes the interferences from the thin cirrus, stratospheric WV anomaly, and overshooting tops. This conclusion is also verified by a majority of other cases.

IV. Theoretical Basis of WIRa # Used in Estimating TC Intensity

A. Feasibility

A series of correlation analysis experiments were performed to assess the intensity estimation of the WIRa #. We only trust the original 6-h resolution BT intensity, not the interpolated 1-h resolution intensity; thus, WIRa # at synoptic hours (00, 06, 12, and 18 UTC) were extracted from the 1-h-resolution derived WIRa # series. These WIRa # samples still cover the entire life cycle of each cyclone from formation to land interaction and/or dissipation and were matched with BT intensities (MSLP) at the current analysis time.

Table II shows the names and IDs of all the 35 TCs used in this paper, along with correlation coefficients between WIRa # and JMA BT intensities (MSLP) for each of the TCs. They range from below 0.35 for Xangsane (200615) to a maximum value greater than 0.90 for Saomai (200608). The correlations are statistically significant at the 0.05 level in a two-tailed t-test for all TCs other than Xangsane (200615), Chebi (200620), Kajiki (200719), and Rammasun (200802). To reduce the noise in the time-series plots, the latest 3-h WIRa # are averaged to replace the raw counts. Compared with the original results, the correlation coefficients with 3-h averages are slightly increased. The most significant improvement is found for Kajiki (200719), whose coefficient rises from 0.49 to 0.59. Decreased coefficients are also found for a few low-correlation coefficient TCs such as Xangsane (200615), whose coefficient decreases from 0.32 to 0.29.

TABLE II
Correlation Coefficients Between Original and 3-h Average WIRa # and JMA MSLP Intensities for Each of the 35 TCs in the Database

TC Name (ID)	original	3-h avg	TC Name (ID)	original	3-h avg
Chanchu(200601)	-0.36	-0.31*	Sinlaku(200813)	-0.82	-0.82
Ewiniar(200603)	-0.58	-0.62	Hagupit(200814)	-0.79	-0.79
Saomai(200608)	-0.90	-0.95	Jangmi(200815)	-0.89	-0.89
Shanshan(200613)	-0.54	-0.55	Choi-wan(200914)	-0.64	-0.64
Xangsane(200615)	-0.32*	-0.29*	Parma(200917)	-0.38	-0.38
Cimaron(200619)	-0.68	-0.67	Melor(200918)	-0.70	-0.70
Chebi(200620)	-0.41*	-0.49*	Lupit(200920)	-0.62	-0.62
Durian(200621)	-0.38	-0.37	Fanapi(201011)	-0.76	-0.81
Utor(200622)	-0.52	-0.53	Malakas(201012)	-0.71	-0.71
Yutu(200702)	-0.79	-0.83	Megi(201013)	-0.62	-0.63
Man-yi(200704)	-0.72	-0.76	Chaba(201014)	-0.76	-0.76
Usagi(200705)	-0.78	-0.78	Songda(201102)	-0.68	-0.74
Sepat(200708)	-0.78	-0.76	Ma-on(201106)	-0.36	-0.33*
Nari(200711)	-0.73	-0.77	Muifa(201109)	-0.68	-0.68
Wipha(200712)	-0.66	-0.73	Nanmadol(201111)	-0.68	-0.74
Krosa(200715)	-0.77	-0.79	Roke(201115)	-0.75	-0.76
Kajiki(200719)	-0.49*	-0.59*	Nalgae(201119)	-0.68	-0.71
Rammasun(200802)	-0.40*	-0.43*			

* Correlation is not statistically significant at the 5% level in a two-tailed t-test.

Fig. 6 presents the details to describe how well the 3-h average WIRa # matches with the BT MSLP values for each of the 35 TCs. In general, the variation of WIRa # coincides well with the time series of TC intensities. Xangsane (200615), Cimaron (200619), Utor (200622), and Megi (201013) all experienced a second period of intensification, which is successfully and timely identified by the WIRa #, no matter whether their correlation is statistically significant or not. Note that Megi (201013) was missed by the WIRa # at its peak intensity, which is due to the poor quality of WV-IRW imageries. We have examined the low-correlation coefficient TCs and found that Durian (200621), Parma (200917), and Ma-on (201106) also have the WV-IRW quality problem (the figure evidence and detailed analysis are provided in Section V-C). The low correlation for Xangsane (200615) is probably due to the expertise levels of TC forecasters and satellite analysts. An eye appeared at 18 h after Xangsane's formation (00:00 UTC on 26 September 2006), and the clear eye region and symmetrical inner-core region could be seen at 30 h from the imagery, but the corresponding JMA BT MSLPs at 18 and 30 h are 970 and 940 hPa, respectively. Moreover, Xangsane's intensities estimated by JMA also deviated from those by JTWC. The MSLP of Xangsane at 18:00 UTC 27 September 2006 is estimated to be 960 hPa by JMA, whereas it is 922 hPa by JTWC, with the difference in the estimated MSLP as large as 38 hPa. Chanchu (200601) is an exceptional case. Before its rapid intensification, a widespread cirrus canopy had appeared around the center region. The brightness temperatures of the cirrus canopy are approximately 205 K and severely interfered with the WIRa #.

To understand the overall performance regarding the relationship between the WIRa # and BT MSLP intensities, a scatterplot for all the 35 TC cases is provided in Fig. 7. Note that the correlation coefficient can reach -0.66. This is an averaged value from 35 TCs where both strong and weak relationships occurred.

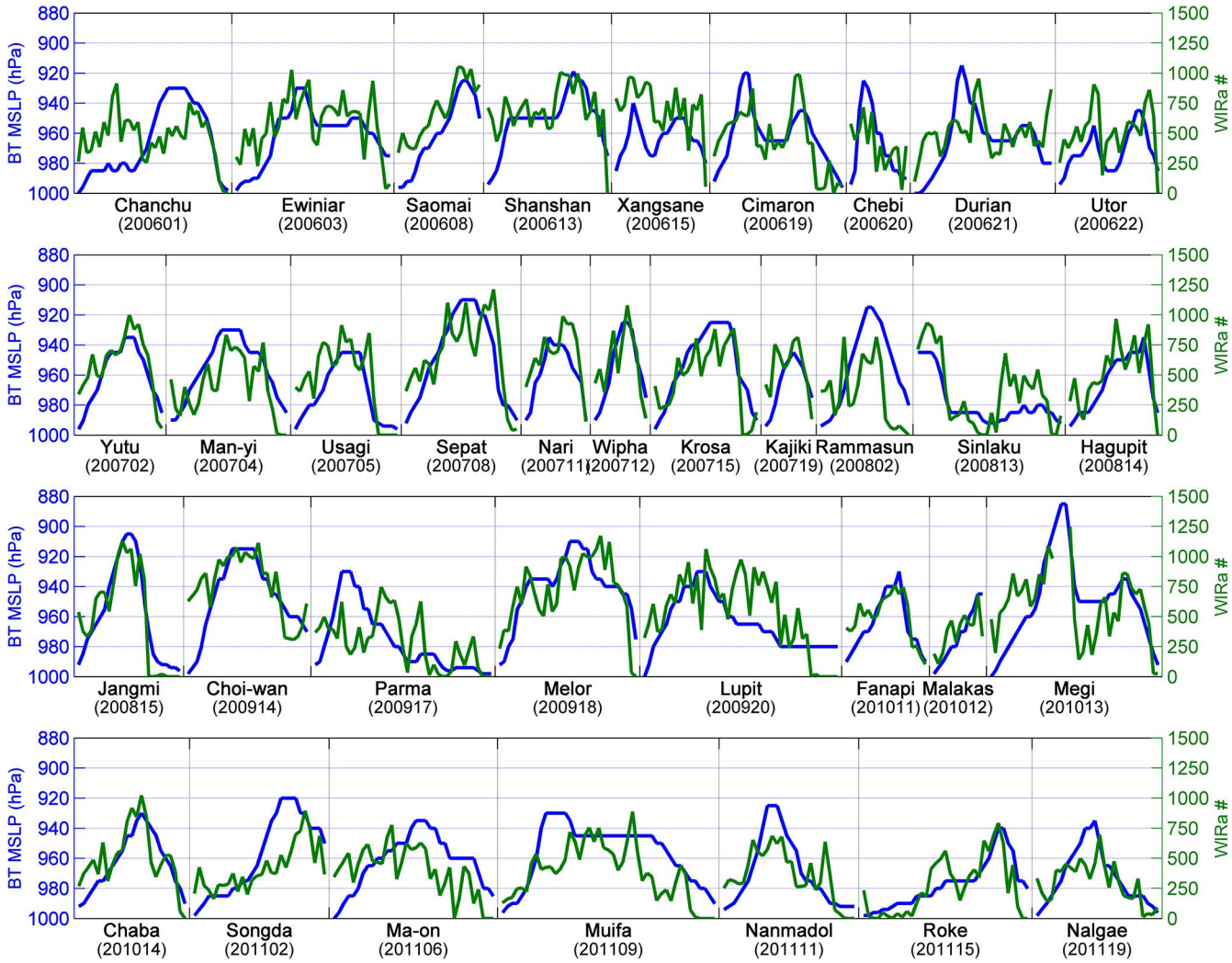

Fig. 6. Time-series plots of (dark green lines) 3-h average WIRa # versus (blue lines) BT MSLP measurements for each of the 35 TCs.

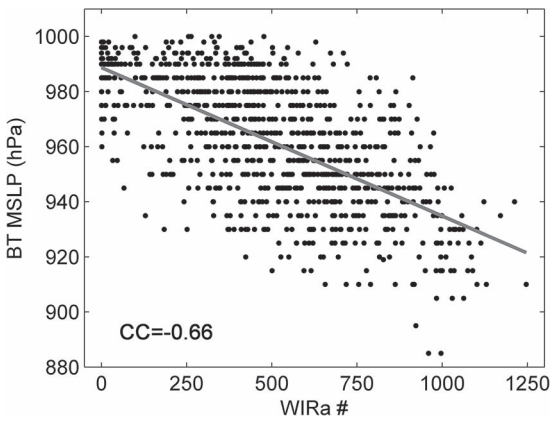

Fig. 7. Scatterplot showing the correlation between 3-h average WIRa # and BT intensities (MSLP) for all the 35 TC cases. The gray solid line indicates the linear regression best fit.

TABLE III
CORRELATION COEFFICIENTS BETWEEN THE BRIGHTNESS TEMPERATURE PARAMETERS AND COINCIDENT BT INTENSITIES (MSLP) FOR THE FIVE 6-h LAG PERIODS BETWEEN 0 AND 24 h, INCLUSIVE. THE CORRELATION COEFFICIENTS WITH ABSOLUTE VALUES ABOVE 0.60 ARE SHOWN IN BOLDFACE

	No lag	6-h lag	12-h lag	18-h lag	24-h lag
Mean Tb_{IRW}	0.46	0.52	0.55	0.56	0.55
Tb_{WV-IRW} >0K	-0.49	-0.56	**-0.60**	**-0.61**	-0.59
1.5K>= Tb_{WV-IRW} >0K	-0.57	**-0.60**	-0.59	-0.55	-0.49
Tb_{WV-IRW} >1.5K	-0.23	-0.33	-0.39	-0.44	-0.46
Tb_{IRW} <=215K	-0.50	-0.57	**-0.60**	-0.59	-0.57
200K< Tb_{IRW} <=215K	-0.41	-0.35	-0.28	-0.19	-0.11
Tb_{IRW} <=200K	-0.29	-0.38	-0.45	-0.49	-0.51
WIRa #	**-0.66**	**-0.64**	-0.59	-0.50	-0.40
No.of comparisons	930	895	860	825	790

B. Comparison Test

To compare with WIRa #, several brightness temperature parameters usually used in operational TC intensity estimation and forecast were also examined. These parameters were matched with BT intensities (MSLP) at the current analysis time, as well as four additional 6-h time-lag increments (i.e., future 6, 12, 18, and 24 h). Table III presents the correlation coefficients of these brightness temperature parameters for each of the five individual 6-h time-lag periods. The first row is for the mean value of Tb_{IRW}, which is used within both the subjective DT and objective satellite-based algorithms (e.g., ODT, AODT, and ADT). The following three rows contain

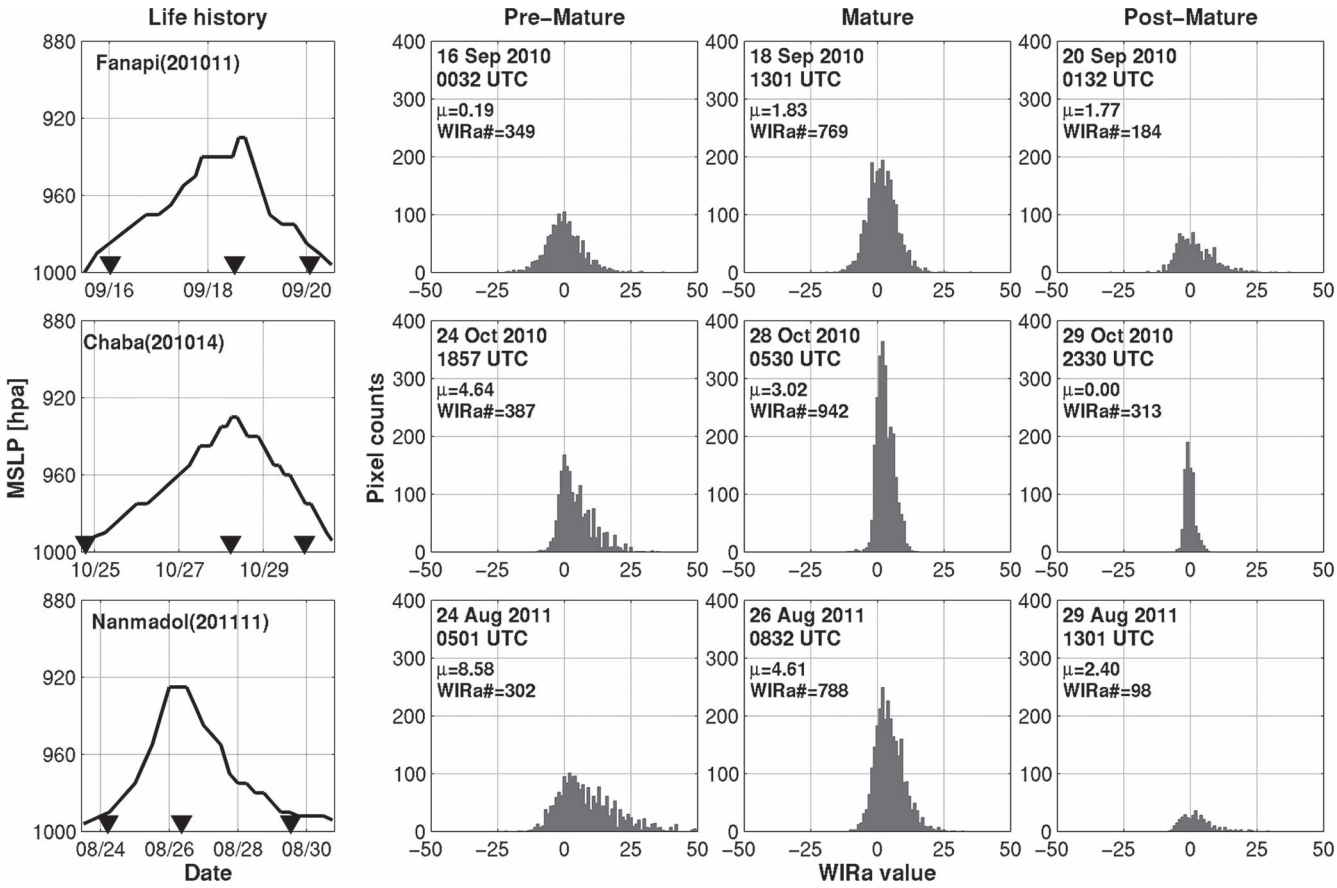

Fig. 8. (First column) TC life history and WIRa distributions in the TC (second column) premature stage, (third column) mature stage, and (fourth column) post-mature stage. One histogram is for one MTSAT image, and the analysis time corresponded is indicated by downward-pointing triangles in the life history plots. The WIRa mean value μ and the WIRa # are labeled in each of the nine histograms on the left side.

parameters relevant to $Tb_{\mathrm{WV-IRW}}$. The second row counts the pixels with $Tb_{\mathrm{WV-IRW}} > 0$ K. Same as the statistical result in [25], the pixel count of $Tb_{\mathrm{WV-IRW}} > 0$ K possesses higher correlation values in the 18- and/or 24-h lag periods but remains a low-correlation value at the current analysis time (i.e., in no-lag periods). However, if only the pixels with $1.5 \text{ K} \geq Tb_{\mathrm{WV-IRW}} > 0$ K are considered (see the third row of Table III), a majority of overshooting convection and stratospheric WV anomaly pixels are excluded and the pixel counts display a higher correlation with the BT current intensities. On the contrary, if only the pixels with $Tb_{\mathrm{WV-IRW}} > 1.5$ K are considered, (see the fourth row of Table III), the correlation between pixel counts and BT current intensities is very weak but increases as the lag period increases. Rows 5–7 contain elements relevant to Tb_{IRW}, which also display low correlation with current intensities but increased correlation with future intensities if overshooting convection pixels are included. The eighth row is the WIRa # proposed in this paper, and it possesses the highest correlation value with current intensities and decreased correlations with future intensities.

Overshooting convection can occur in any stages of the life cycle, including the cyclogenesis stage [41]–[43]. The overshooting convection is of very short duration. However, benefiting from the latent heating released by overshooting convection, TC often intensifies rapidly and reaches a strong intensity in the next 12 or 24 h. Therefore, it is rational to use overshooting convection to forecast TC's future intensity, and this is why Olander and Velden [25] succeed with the pixel count of $Tb_{\mathrm{WV-IRW}} > 0$ K. However, the overshooting convection is interference information for current intensity estimation (at least, the relationship between overshooting convection and current intensities is not close), and thus, WIRa # has a closer relationship with the current intensities after excluding the overshooting top's obscuring effects.

C. Further Meteorological Interpretation

The time series of WIRa # for a particular cyclone are found to be correlated with the MSLP. The higher is the WIRa # at a particular time, the lower is the MSLP (i.e., the more intense is the TC) at that time. The WIRa # increases for two possible reasons: 1) the number of pixels meeting the threshold of $Tb_{\mathrm{IRW}} < 215$ K increases; and 2) the number of pixels with $Tb_{\mathrm{IRW}} < 215$ K is roughly unchanged, but the scatter of pixel-level WIRa values becomes tighter (i.e., the standard deviation of WIRa decreases). We can further illustrate this phenomenon with the help of Fig. 8. As shown in Fig. 8, the total number of deep convection and cirrus pixels increases when TC is developing (i.e., the TC is from the genesis to the mature stage) and decreases when TC is weakening (i.e., the TC is from the

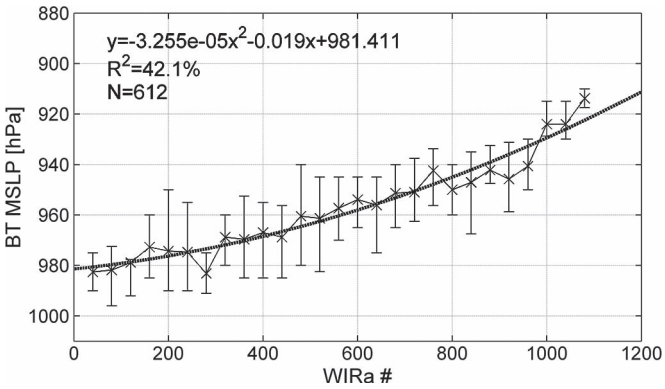

Fig. 9. Distribution of intensities and the WIRa # for 22 cases (66% of available records) randomly chosen from 35 TCs. For each error bar, the cross sign represents the mean value and the whiskers extend out to the 75% and 25% percentile. Dashed line indicates the regression-based relationship. R^2 is the variance explained.

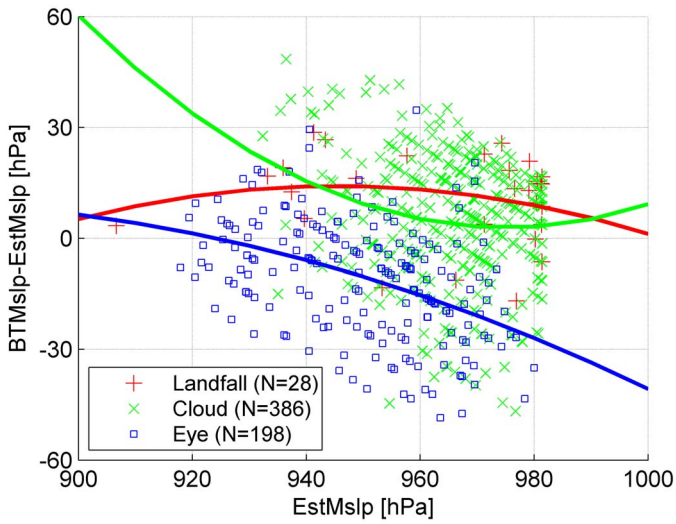

Fig. 10. Scene-type bias adjustment. BTMslp and EstMslp represent the intensity (MSLP) from BT data set and with the regression equation, respectively.

mature stage to the dissipative stage), meaning that the pixel count of $Tb_{\mathrm{IRW}} < 215$ K can display the convective vigor's variation. In addition, WIRa distribution appears normal-like, although the shapes of distribution curves vary with different TCs and at different stages of their life cycle. WIRa moves toward the mean value μ for a developing TC, indicating that the values of inner-core Tb_{IRW} and/or $Tb_{\mathrm{WV-IRW}}$ tend to be uniform and the eyewall is becoming more symmetric. Accordingly, WIRa departs from μ for a weakening TC, and the eyewall is becoming asymmetric. In view of this, the WIRa-based indicator can simultaneously display the convection's symmetrization level and vigor, which are the two conventional approaches for estimating TC intensity with geostationary satellite imagery.

V. Results

A. Best Fit Relationship

The regression equation between TC intensities and the WIRa # is generated using a training set of 22 cases (approximately 66% of the available records) randomly chosen from 35 TCs. This training set did not include Sinlaku (200813), Jangmi (200815), Fanapi (201011), Malakas (201012), and Megi (201013) because these five TCs would be used in the evaluation (see Section V-B). Finally, the regression equation is quadratic and shown in Fig. 9. According to this equation, when WIRa # is equal to 0, all of the inner-core pixels are with $Tb_{\mathrm{IRW}} > 215$ K and/or $Tb_{\mathrm{WV-IRW}} < 0$ K, and at this time, the estimated MSLP would be 981.41 hPa, indicating that the cyclone intensities below severe tropical storm strength would be overestimated (i.e., the MSLP estimates are lower than observation). In addition, the cyclone intensities above category 5 are possibly underestimated (i.e., the MSLP estimates are higher than observation) because the estimated intensity is still greater than 910 hPa with WIRa # equal to 1200.

Gaining enlightenment from the ADT method that conducts a scene-type determination before intensity estimation and ensures that MSLP is lower than 960 hPa for Eye scene types and greater than 940 hPa for non-Eye scene types, a scene-type bias adjustment is conducted in this paper. Here, all records were manually divided into three scene types, namely, Eye, Cloud, and Landfall according to its IRW feature. When an eye is present on the IRW imagery, the record is determined as Eye scene type and, otherwise, Cloud scene type. If the storm makes landfall, the record is determined as Landfall scene type no matter whether this storm has an eye or not. The scatterplot of these three scene types is presented in Fig. 10. It is shown that the intensity may be underestimated for Eye scene type but overestimated for Cloud scene type. On this account, the scene-type bias adjustment is conducted by using the following equations:

TABLE IV
Evaluation Results for the Regression Equation Using 13 TC Cases. Units Are All in Hectopascals. (BA = Bias Adjustment; cc = Correlation Coefficient)

	Avg(*BTMslp*)	Avg(*EstMslp*)	bias	MAE	RMSE	cc
Pre-BA	965.49	963.11	-2.38	12.30	15.14	0.65
Post-BA	965.49	961.95	-3.54	10.52	13.00	0.78

$$\mathrm{EstMslp}_{\mathrm{post-BA}} = \mathrm{EstMslp}_{\mathrm{pre-BA}} + \begin{cases} -0.0044 \cdot \mathrm{EstMslp}^2_{\mathrm{pre-BA}} + 8.23 \cdot \mathrm{EstMslp}_{\mathrm{pre-BA}} - 3876.73 & \text{Eye} \\ 0.0102 \cdot \mathrm{EstMslp}^2_{\mathrm{pre-BA}} - 19.89 \cdot \mathrm{EstMslp}_{\mathrm{pre-BA}} + 9697.75 & \text{Cloud} \\ -0.0027 \cdot \mathrm{EstMslp}^2_{\mathrm{pre-BA}} + 4.73 \cdot \mathrm{EstMslp}_{\mathrm{pre-BA}} - 2032.67 & \text{Landfall} \end{cases} \quad (2)$$

where $\mathrm{EstMslp}_{\mathrm{pre-BA}}$ and $\mathrm{EstMslp}_{\mathrm{post-BA}}$ represent the estimated TC intensity before and after the scene-type bias adjustment, respectively.

TABLE V
FOURTEEN DROPSONDE OBSERVATIONS VERSUS THE INTENSITY ESTIMATES DERIVED FROM DIFFERENT METHODS. UNITS ARE ALL IN HECTOPASCALS. (DRPS = DROPSONDE MEASUREMENTS; BA = BIAS ADJUSTMENT)

Drps. Time (UTC)	TC ID	Drps.	WIRa-based		BT		ADT		
			Pre-BA	Post-BA	JMA	JTWC	CI#	Adjusted T#	raw T#
06:09 10/Sep/2008	200813	954	NaN	NaN	944.55	936.65	962.4(4.7)	933.7(5.8)	925.5(6.1)
16:50 12/Sep/2008	200813	954	944.08	944.08	944.89	946.26	941.0(5.5)	943.6(5.4)	943.6(5.4)
03:18 18/Sep/2008	200813	979	969.33	973.96	979.76	979.31	991.6(2.8)	988.2(3.2)	983.5(3.5)
05:24 20/Sep/2008	200813	997	977.72	982.92	991.8	981.87	986.3(3.1)	986.5(3.2)	986.5(3.2)
01:29 26/Sep/2008	200815	979	950.95	940.15	959.25	954.94	953.7(5.1)	985.3(3.6)	985.3(3.6)
09:28 27/Sep/2008	200815	905	923.79	923.51	906.27	917.49	902.1(6.9)	902.1(6.9)	902.1(6.9)
02:58 16/Sep/2010	201011	979	969.94	976.73	982.63	979.71	983.2(3.6)	983.2(3.6)	994.4(3.0)
02:52 17/Sep/2010	201011	968	961.72	968.32	968.77	965.24	970.5(4.3)	959.0(4.8)	954.3(5.0)
01:17 18/Sep/ 2010	201011	940	954.42	941.61	940.24	946.64	924.6(6.1)	923.9(6.2)	923.9(6.2)
18:52 24/Sep/2010	201012	957	952.20	945.09	944.08	947.48	935.9(5.6)	923.5(6.2)	923.5(6.2)
04:14 14/Oct/2010	201013	986	965.97	970.67	991.76	979.59	981.2(3.9)	981.2(3.9)	984.4(3.7)
03:34 16/Oct/2010	201013	963	959.90	966.82	957.6	951.6	965.6(4.6)	965.6(4.6)	982.8(3.8)
23:42 16/Oct/2010	201013	918	921.59	921.26	915.41	918.3	899.7(7.0)	899.7(7.0)	899.7(7.0)
13:08 17/ Oct/2010	201013	890	NaN	NaN	893	902.74	884.7(7.4)	884.7(7.4)	884.7(7.4)

B. Evaluation

Thirteen TCs are used for a simple evaluation. The evaluation indices of bias, mean absolute error (MAE), and root-mean-square error (RMSE) are defined as

$$\text{bias} = \frac{1}{N}\sum_{i=1}^{N}(\text{EstMslp}_i - \text{BTMslp}_i) \tag{3}$$

$$\text{MAE} = \frac{1}{N}\sum_{i=1}^{N}|\text{EstMslp}_i - \text{BTMslp}_i| \tag{4}$$

$$\text{RMSE} = \sqrt{\frac{1}{N}\sum_{i=1}^{N}(\text{EstMslp}_i - \text{BTMslp}_i)^2}. \tag{5}$$

In (3)–(5), N indicates the record number, EstMslp represents the intensity (MSLP) estimated by WIRa #, and BTMslp represents BT intensity (MSLP). The evaluation results for the equation are listed in Table IV. The MSLP estimate errors significantly decrease after the scene-type bias adjustment. Moreover, the correlation coefficient between the estimated and BT intensities reaches 0.78 after bias adjustment, whereas it is 0.65 without the bias adjustment.

The WIRa-based intensity estimates (before/after the bias adjustment) are also compared with JMA BT intensity, JTWC BT intensity (http://www.usno.navy.mil/NOOC/nmfc-ph/RSS/jtwc/best_tracks/index.html), ADT-derived intensity (http://tropic.ssec.wisc.edu/misc/adt/), and dropsonde observations. Tens of dropsondes still fell in the TC eye regions during the TPARC/TCS-08 and ITOP/TCS-10 after the global aircraft reconnaissance program deactivated since 1987. If there is more than one dropsonde measurement in a short time, the one with the lowest value and/or nearest the JMA BT determined center is chosen as the truth. Finally, 14 observations are picked out and listed in Table V, accompanied by intensity estimates derived from different methods. Note that the WIRa-based estimates in the first and last lines are invalid due to the missing satellite data or poor imagery quality as aforementioned, and thus, 12 observations are available.

TABLE VI
STATISTIC FOR 12 AVAILABLE OBSERVATIONS. UNITS ARE ALL IN HECTOPASCALS. Avg(Drps) = 960.42 hPa. THE ABBREVIATION IS SAME AS IN TABLE V

	WIRa-based		BT		ADT		
	Pre-BA	Post-BA	JMA	JTWC	CI#	Adj. T#	raw T#
Avg	954.30	954.56	956.87	955.70	952.95	953.48	955.33
bias	-6.12	-5.86	-3.55	-4.71	-7.47	-6.93	-5.08
MAE	12.25	10.45	5.62	8.12	11.12	10.65	12.75
RMSE	14.38	14.70	7.92	10.56	13.42	13.53	15.34

The comparison results are completely summarized in Table VI. JMA/JTWC BT intensities display the smallest biases and RMSEs due to assimilating the dropsonde and other aircraft measurements, whereas the WIRa-based intensities produce a 12.25-hPa MAE before the scene-type bias adjustment and a 10.45-hPa MAE after scene-type bias adjustment, which are slightly worse than the BT estimates. This is understandable because the BT data set was regarded as the validation data for the regression equation, and the WIRa-based algorithm is dependent upon the BT intensity accuracy of the training samples.

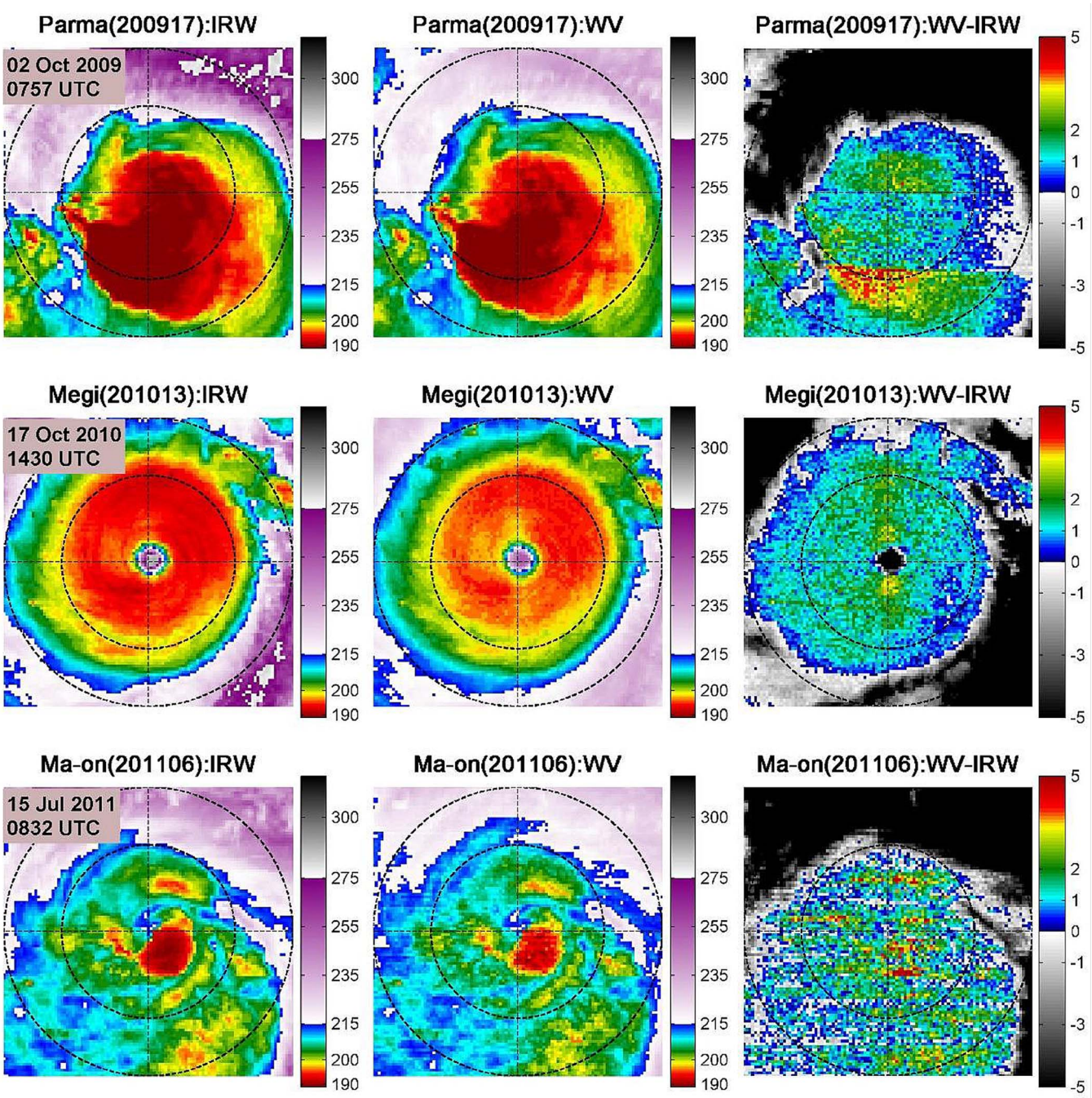

Fig. 11. Examples for (left) IRW, (middle) WV, and (right) WV-IRW imageries contaminated by belt-shaped scan anomalies. Cycles with dashed line mark radii of 150 and 250 km, respectively. Units are all in kelvin for the colorbar.

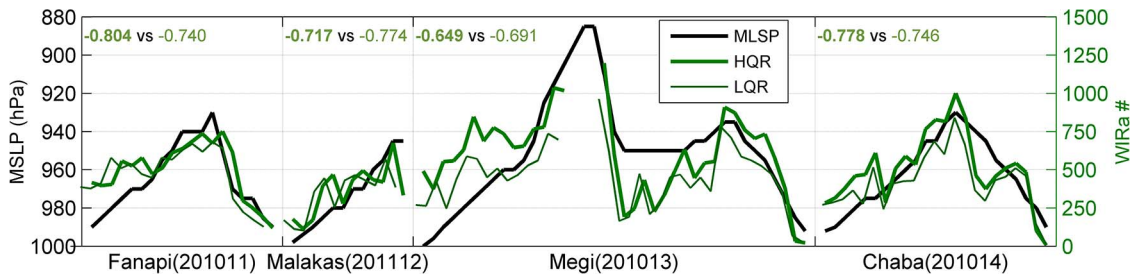

Fig. 12. Homogeneous comparisons between the WIRa # calculated with high-resolution (1024-gradation) imagery (HQR) and those with low-resolution (256-gradation) imagery (LQR). Green numbers indicate their correlation coefficients with BT intensities (MSLP).

The ADT CI# intensity estimate has an 11.12-hPa MAE and a 13.42-hPa RMSE from the dropsonde measurements and is close to the statistics using 1116 Atlantic reconnaissance cases from 1996 to 2005 in [20]. An assertion that the WIRa-based method is competitive with the ADT method can be made without further comparison to the ADT raw T# or adjusted T# intensity estimates.

C. Factors Influencing the Estimation Accuracy

According to (1), a 1-K increment (or decrement) of Tb_{IRW} results in a WIRa variation of 1 when setting $Tb_{\mathrm{WV-IRW}}$ to 2 K, but a 1-K increment (or decrement) of $Tb_{\mathrm{WV-IRW}}$ can bring a WIRa variation of 5, which generates an unacceptable bias in the WIRa # when setting Tb_{IRW} to 200 K. Therefore, the estimation accuracy of the WIRa-based method relies on the quality of WV-IRW imagery.

The unreasonable increment or decrement in brightness temperatures is named "scan anomaly" here. Although a scan anomaly of 1 K on the IRW or WV imagery can be regarded as a common noise and hence ignored, it is extremely obvious on WV-IRW imagery. The frequency of scan anomalies increases as the satellite instruments age. The anomalies are generally belt-shaped and distribute along the south–north or east–west direction. They are wide and sparse on MTSAT-1R imagery, whereas they are narrow and dense on MTSAT-2 imagery. WIRa-based method is contaminated or even becomes useless when the TC inner-core region is influenced by scan anomalies. As shown in Fig. 11, on the imagery of Parma (200917) at 08:00 UTC on 2 October 2009, nearly half of the inner core was covered by a belt along the east–west direction with a width of 130 km. On 17 October 2010, when Megi (201013) was at its peak intensity, a belt along the south–north direction crossed Megi's eye region and stayed there for almost one day, leading to the suspicious WIRa estimates. Worse is Ma-on (201106), which was constantly contaminated by the belt-shaped anomalies during its entire life cycle. The scan anomalies actually appear to be more frequent and ubiquitous on MTSAT-2 imagery, and nearly all the imageries of TCs in 2011 were affected.

Another factor influencing the estimation accuracy is the quantization resolution. The quantization resolution determines the diacritic brightness temperature interval in calibration tables/equations, and thus, more precise $Tb_{\mathrm{WV-IRW}}$ can be identified from the imagery with a higher quantization resolution. A quantization resolution reduction often occurs in the data distribution and storage. For example, the original calibration table of MTSAT is 1024-gradation (as used in this paper); however, to save storage space, this table is reduced to 256-gradation by Kochi University (http://weather.is.kochi-u.ac.jp/archive-e.html). Fig. 12 displays the homogeneous comparisons between the WIRa # calculated with high-resolution (1024-gradation) imagery and those with low-resolution (256-gradation) imagery. It is shown that the WIRa # values and corresponding correlation coefficients computed with different-resolution imagery are not completely consistent.

VI. Discussion and Conclusion

The new parameter WIRa proposed in this paper can combine the information of WV-IRW and IRW imageries. Based on this combined information, the pixels with WIRa between the range of $[\mu, \mu + 5]$ and under the constraint of $Tb_{\mathrm{IRW}} < 215$ K are counted and correlated with JMA BT intensities (MSLP). Abundant tests and results show that the WIRa-based indicator not only can screen out the thin cirrus, stratospheric WV anomaly, and overshooting tops that are irrelevant with TC current intensities but also is able to illustrate the convection's symmetrization level and vigor within the TC inner-core region. The WIRa-based indicator gives a more accurate estimation of TC intensities when compared with other geostationary satellite-based indicators.

The storm center and scene-type determination schemes of DT methods are referred to in the process of TC intensity estimation with the WIRa-based method. Therefore, this paper has no intention to replace the existing DT methods with the WIRa-based method. This WIRa-based method may provide an additional parameter within the current ADT regression equations, and thus may be an important supplement or modification to the DT methods.

Obviously there still exists room for improvements of the WIRa-based method based on the following reasons. First, the TC inner-core size is fixed to 150 km in this paper, which is very limited. In fact, the inner-core size varies from 50 km [e.g., Ruth (197702)] to 500 km [e.g., Tip (197920)]. The wide range of TC inner-core size should be considered in further research. Second, current WIRa-based method depends on the accuracy of BT data set since it is used as validation data when the regression equation is created. The WIRa-based method will be further improved if the intensity estimation equation can be calculated with the Atlantic reconnaissance measurements and the European (American) geostationary satellite imagery.

Appendix
IRW and WV-IRW's Sensitivity to Clouds and Atmospheric Parameters

The model used for analyzing the sensitivity of IRW and WV-IRW to clouds and atmospheric parameters is the Santa Barbara discrete ordinate radiative transfer Atmospheric Radiative Transfer (SBDART). SBDART is a software tool that includes all the important processes affecting the ultraviolet, visual, and infrared radiation transfer [45]. SBDART can rapidly compute plane–parallel radiative transfer in clear and cloudy conditions [46], [47] and is widely applied in various radiation and remote sensing studies [48]–[50].

In this section, SBDART with a background stratospheric aerosol type and an oceanic boundary layer aerosol type with horizontal visibility of 23 km at 0.55 μm are used. The observation altitude is at 100 km, and the solar radiation is ignored. The environmental field is prescribed using tropical atmospheric profiles [51], but relative humidity within clouds is set to 90%. Note that the cold-point tropopause is at a 90-hPa altitude (about 17 km) with a temperature of 195 K.

TABLE VII
BRIGHTNESS TEMPERATURE DIFFERENCES PRODUCED BY CLOUDS WITH DIFFERENT CTHs. UNITS ARE ALL IN KELVIN

	6.5μm	11.0μm	6.5-11.0μm
CTH=13km	217.14	218.23	-1.08
CTH=14km	211.50	211.53	-0.03
CTH=15km	206.40	205.54	0.86
CTH=16km	200.99	199.11	1.88
CTH=17km	198.15	195.75	2.40
CTH=18km	199.78	197.68	2.10
CTH=21km	210.35	209.32	1.03
CTH=23km	217.21	216.48	0.74

A. Basic Experiment

The impact of cloud top height (CTH) on $Tb_{\mathrm{WV-IRW}}$ is studied. A developed ice-phase cloud extends from 6 km to a high altitude with a total optical thickness (at 0.55 μm) of 40 and an ice effective radius of 35 μm. The model results for the radiance with different CTHs (from 13 to 23 km) are shown in Table VII. In the troposphere, Tb_{WV} and Tb_{IRW} decrease with CTH's increase, but $Tb_{\mathrm{WV-IRW}}$ increases and turns positive at 14.1 km (with the environmental temperature of about 210 K). When the CTH breaches into the tropopause (up to 18 km), Tb_{WV} and Tb_{IRW} increase again, and $Tb_{\mathrm{WV-IRW}}$ decreases. However, the decreasing rate of $Tb_{\mathrm{WV-IRW}}$ is insignificant. Even if the CTH is 23 km with an environmental temperature of 216 K (in fact, cloud with $\mathrm{CTH} = 23$ km is very rare), $Tb_{\mathrm{WV-IRW}}$ is still 0.7 K. Results in Table VII clearly indicate that $Tb_{\mathrm{WV-IRW}}$ is always positive once the cloud top reaches a certain height, no matter whether it is overshooting into the stratosphere or not.

B. WV Anomaly Experiment

The active thunderstorm updraft and other sources can result in the WV amount's sudden increment above cloud top (i.e., WV anomaly). Here, the extreme cases are studied. The CTH is fixed, and WV at a certain level in the tropical atmospheric profile (i.e., environmental field) is adjusted to saturation. The parameters for clouds are the same as those in the basic experiment. Table VIII shows that Tb_{IRW} remains unchanged as in the basic case when the environmental WV changes. When the saturated WV level (SWVL) is below the cloud top, the value of $Tb_{\mathrm{WV-IRW}}$ does not change. However, when the saturated WV is above the cloud top and both CTH and SWVL are below the tropopause, $Tb_{\mathrm{WV-IRW}}$ will decrease, but if the saturated WV is above the cloud top and SWVL is in the stratosphere, $Tb_{\mathrm{WV-IRW}}$ will increase. The brightness temperature difference will be remarkable if the stratospheric saturated WV's temperature is much higher than the cloud top temperature (as shown in the last line of Table VIII). Accordingly, if a strong thermal inversion occurs in the lower stratosphere, the WV can generate a greatly positive $Tb_{\mathrm{WV-IRW}}$ without being transported to a high altitude [52].

C. Thin Cirrus Experiment

A cirrus cloud between 15 and 16 km is set. This cirrus is with a constant ice effective radius of 35 μm but a variable thickness. The optical thickness (at 0.55 μm) is set to 1, 5, and 10, respectively. Three scenarios below the cirrus are considered: 1) a clear sky (SCEN100); 2) a water-phase cloud extending from 1 to 5 km with a total optical thickness (at 0.55 μm) of 40 and a droplet effective radius of 15 μm (SCEN101); and 3) an ice-phase cloud extending from 6 to 15 km with a total optical thickness (at 0.55 μm) of 40 and an ice effective radius of 30 μm (SCEN110). Table IX indicates that Tb_{WV} and Tb_{IRW} of the cirrus are affected by the radiance below. The influence will be more remarkable if the cirrus is optically thinner. When it is clear sky (SCEN100) or a low cloud (SCEN101) below the thin cirrus, Tb_{IRW} will be higher than the cloud temperature, and $Tb_{\mathrm{WV-IRW}}$ will be significantly negative or weakly positive. If the cirrus is optically thick or there is a high cloud (SCEN110) below the cirrus, the radiative characteristic of the cirrus is quite similar to that of the convective clouds whose top is at the same height. This indicates that thin cirrus in SCEN100 or SCEN101 can be recognized from infrared imagery with Tb_{IRW} or $Tb_{\mathrm{WV-IRW}}$ if the CTH is known, but it is very difficult to recognize thick cirrus or cirrus in SCEN110.

The radiative characteristic of stratospheric cirrus is similar to that of troposphere cirrus (table omitted).

TABLE VIII
BRIGHTNESS TEMPERATURE DIFFERENCES PRODUCED BY TROPICAL ATMOSPHERIC PROFILES WITH DIFFERENT SWVLs. UNITS ARE ALL IN KELVIN. (REF=REFERENCE PROFILE EXTRACTED FROM TABLE VII)

		6.5μm	11.0μm	6.5-11.0μm
CTH=16km	Ref	200.99	199.11	1.88
	SWVL=16km	200.98	199.11	1.87
	SWVL=17km	200.97	199.11	1.86
	SWVL=18km	201.00	199.11	1.89
	SWVL=21km	202.77	199.11	2.66
CTH=17km	Ref	198.15	195.75	2.40
	SWVL=16km	198.15	195.75	2.40
	SWVL=17km	198.16	195.75	2.41
	SWVL=18km	198.22	195.75	2.47
	SWVL=21km	199.16	195.75	3.41

TABLE IX
BRIGHTNESS TEMPERATURE DIFFERENCES PRODUCED BY THE CIRRUS WITH DIFFERENT OPTICAL THICKNESSES AT 0.55 μm (TAU) AND IN DIFFERENT SCENES. UNITS ARE ALL IN KELVIN

		6.5μm	11.0μm	6.5-11.0μm
Tau=1	SCEN100	220.65	253.92	-33.27
	SCEN101	220.65	238.40	-17.75
	SCEN110	203.76	202.34	1.41
Tau=5	SCEN100	202.26	203.98	-1.72
	SCEN101	202.26	201.97	0.29
	SCEN110	200.62	198.68	1.95
Tau=10	SCEN100	199.90	197.97	1.93
	SCEN101	199.90	197.90	2.01
	SCEN110	199.85	197.79	2.06

D. Microphysics Experiment

A deep ice-phase cloud is set. The "cloud body" extends from 6 to 15 km with a total optical thickness (at 0.55 μm) of 40 and an ice effective radius of 30 μm. The "cloud top" is from 15 to

TABLE X
BRIGHTNESS TEMPERATURE DIFFERENCES PRODUCED BY CLOUDS WITH DIFFERENT OPTICAL THICKNESSES AT 0.55 μm (TAU) AND ICE EFFECTIVE RADIUS (RE_I). UNITS ARE ALL IN KELVIN

		6.5μm	11.0μm	6.5-11.0μm
Re_i=35μm	Tau=0.1	205.94	205.07	0.88
	Tau=1	203.76	202.34	1.41
	Tau=5	200.62	198.68	1.95
	Tau=10	199.85	197.79	2.06
	Tau=30	199.34	197.20	2.14
	Tau=50	199.24	197.08	2.16
Tau=10	Re_i=15μm	199.70	197.68	2.01
	Re_i=35μm	199.85	197.79	2.06
	Re_i=55μm	199.89	197.83	2.06
	Re_i=100μm	199.92	197.87	2.05

16 km. The optical thickness and ice effective radius' impact on $Tb_{\mathrm{WV-IRW}}$ is studied (see Table X). $Tb_{\mathrm{WV-IRW}}$ increases when "cloud top" ice effective radius increases from 15 to 35 μm but decreases when the ice effective radius continues to increase. Even so, the ice radius' impact is weak because the variational amplitude of $Tb_{\mathrm{WV-IRW}}$ is less than 0.5 K. The optical thickness' impact is more obvious compared with that of the ice effective radius. When the "cloud top" is extremely thin (with an optical thickness of 0.1), most radiation is controlled by the "cloud body." $Tb_{\mathrm{WV-IRW}}$ increases as the cloud top's thickness increases. $Tb_{\mathrm{WV-IRW}}$ tends to be constant after the optical thickness breaches 10.

ACKNOWLEDGMENT

The authors would like to thank Dr. J. Xiao and Dr. J.-F. Gu of School of Atmospheric Sciences, Nanjing University for numerous helpful discussions and suggestions. Suggestions from three anonymous reviewers greatly contributed to improving the manuscript.

REFERENCES

[1] C. S. Velden, B. Goodman, and R. Merrill, "Western North Pacific tropical cyclone intensity estimation from NOAA polar-orbiting satellite microwave data," *Mon. Weather Rev.*, vol. 119, no. 1, pp. 159–168, Jan. 1991.

[2] R. L. Bankert, and P. M. Tag, "An automated method to estimate tropical cyclone intensity using SSM/I imagery," *J. Appl. Meteorol.*, vol. 41, no. 5, pp. 461–472, May 2002.

[3] K. F. Brueske, and C. Velden, "Satellite-based tropical cyclone intensity estimation using the NOAA-KLM Series Advanced Microwave Sounding Unit (AMSU)," *Mon. Wea. Rev.*, vol. 131, no. 4, pp. 687–697, Apr. 2003.

[4] J. S. Griffin, R. W. Burpee, F. D. Marks, and J. L. Franklin, "Real-time airborne analysis of aircraft data supporting operational hurricane forecasting," *Wea. Forecast.*, vol. 7, no. 3, pp. 480–490, Sep. 1992.

[5] C.-C. Wu *et al.*, "Dropwindsonde observations for typhoon surveillance near the Taiwan region (DOTSTAR): An overview," *Bull. Amer. Meteorol. Soc.*, vol. 86, no. 6, pp. 787–790, Jun. 2005.

[6] S. D. Aberson *et al.*, "Thirty years of tropical cyclone research with the NOAA P-3 aircraft," *Bull. Amer. Meteorol. Soc.*, vol. 87, no. 8, pp. 1039–1055, Aug. 2006.

[7] K. L. Corbosiero, J. Molinari, and M. L. Black, "The structure and evolution of Hurricane Elena (1985). Part I: Symmetric intensification," *Mon. Wea. Rev.*, vol. 133, no. 10, pp. 2905–2921, Oct. 2005.

[8] K. L. Corbosiero, J. Molinari, A. R. Aiyyer, and M. L. Black, "The structure and evolution of Hurricane Elena (1985). Part II: Convective asymmetries and evidence for vortex Rossby waves," *Mon. Wea. Rev.*, vol. 134, no. 11, pp. 3073–3091, Nov. 2006.

[9] P. T. May, J. D. Kepert, and T. D. Keenan, "Polarimetric radar observations of the persistently asymmetric structure of Tropical Cyclone Ingrid," *Mon. Wea. Rev.*, vol. 136, no. 2, pp. 616–630, Feb. 2008.

[10] C.-K. Yu and L.-W. Cheng, "Radar observations of intense orographic precipitation associated with Typhoon Xangsane (2000)," *Mon. Wea. Rev.*, vol. 136, no. 2, pp. 497–521, Feb. 2008.

[11] C. S. Velden *et al.*, "The Dvorak tropical cyclone intensity estimation technique: A satellite-based method that has endured for over 30 years," *Bull. Amer. Meteorol. Soc.*, vol. 87, no. 9, pp. 1195–1210, Sep. 2006.

[12] J. C. Sadler, "Tropical cyclones of the Eastern North Pacific as revealed by TIROS observations," *J. Appl. Meteorol.*, vol. 3, no. 4, pp. 347–366, Aug. 1964.

[13] S. Fritz, L. F. Hubert and A. Timchalk, "Some inferences from satellite pictures of tropical disturbances," *Mon. Wea. Rev.*, vol. 94, no. 4, pp. 231–236, Apr. 1966.

[14] L. F. Hubert and A. Timchalk, "Estimating hurricane wind speeds from satellite pictures," *Mon. Wea. Rev.*, vol. 97, no. 5, pp. 382–383, May 1969.

[15] V. Dvorak, "Tropical cyclone intensity analysis and forecasting from satellite imagery," *Mon. Wea. Rev.*, vol. 103, no. 5, pp. 420–430, May 1975.

[16] V. Dvorak, "Tropical cyclone intensity analysis using satellite data," NOAA/NESDIS, Washington, DC, USA, NOAA Tech. Rep. NESDIS11, 1984, p. 47.

[17] R. Zehr, "Improving objective satellite estimates of tropical cyclone intensity," in *Proc. 43rd Interdept. Hurricane Conf.*, Homestead AFB, FL, USA, 1989, pp. A-56–A-63.

[18] C. S. Velden, T. L. Olander, and R. M. Zehr, "Development of an objective scheme to estimate tropical cyclone intensity from digital geostationary satellite infrared imagery," *Wea. Forecast.*, vol. 13, no. 1, pp. 172–186, Mar. 1998.

[19] T. L. Olander, C. S. Velden, and M. A. Turk, "Development of the advanced objective Dvorak technique (AODT)—Current progress and future directions," in *Proc. 25th Conf. Hurricanes Tropical Meteorol.*, San Diego, CA, USA, 2002, pp. 585–586.

[20] T. L. Olander and C. S. Velden, "The advanced Dvorak technique: Continued development of an objective scheme to estimate tropical cyclone intensity using geostationary infrared satellite imagery," *Wea. Forecast.*, vol. 22, no. 2, pp. 287–298, Apr. 2007.

[21] T. Nakazawa and S. Hoshino, "Intercomparison of Dvorak parameters in the tropical cyclone datasets over the Western North Pacific," *SOLA*, vol. 5, pp. 33–36, 2009.

[22] C. C. Chao, G. R. Liu, and C. C. Liu, "Estimation of the upper-layer rotation and maximum wind speed of tropical cyclones via satellite imagery," *J. Appl. Meteorol. Climatol.*, vol. 50, no. 3, pp. 750–766, Mar. 2011.

[23] M. F. Piñeros, E. A. Ritchie, and J. S. Tyo, "Objective measures of tropical cyclone structure and intensity change from remotely sensed infrared image data," *IEEE Trans. Geosci. Remote Sens.*, vol. 46, no. 11, pp. 3574–3580, Nov. 2008.

[24] E. A. Ritchie, G. Valliere-Kelley, M. F. Piñeros, and J. Scott Tyo, "Tropical cyclone intensity estimation in the North Atlantic Basin using an improved deviation angle variance technique," *Wea. Forecast.*, vol. 27, no. 5, pp. 1264–1277, Oct. 2012.

[25] T. L. Olander and C. S. Velden, "Tropical cyclone convection and intensity analysis using differenced infrared and water vapor imagery," *Wea. Forecast.*, vol. 24, no. 6, pp. 1558–1572, Dec. 2009.

[26] N. Jaiswal, C. M. Kishtawal, and P. K. Pal, "Cyclone intensity estimation using similarity of satellite IR images based on histogram matching approach," *Atmos. Res.*, vol. 118, pp. 215–221, Nov. 2012.

[27] C. M. Rozoff, W. H. Schubert, B. D. McNoldy, and J. P. Kossin, "Rapid filamentation zones in intense tropical cyclones," *J. Atmos. Sci.*, vol. 63, no. 1, pp. 325–340, Jan. 2006.

[28] Y. Wang, "Rapid filamentation zone in a numerically simulated tropical cyclone," *J. Atmos. Sci.*, vol. 65, no. 4, pp. 1158–1181, Apr. 2008.

[29] W. M. Gray, C. Neumann, and T. L. Tsui, "Assessment of the role of aircraft reconnaissance on tropical cyclone analysis and forecasting," *Bull. Amer. Meteorol. Soc.*, vol. 72, no. 12, pp. 1867–1883, Dec. 1991.

[30] H. Koba, T. Hagiwara, S. Osano, and S. Akashi, "Relationship between the CI-number and central pressure and maximum wind speed in typhoons," *J. Meteor. Res.*, (in Japanese), vol. 42, pp. 59–67, 1990.

[31] H. Jiang, "The relationship between tropical cyclone intensity change and the strength of inner-core convection," *Mon. Wea. Rev.*, vol. 140, no. 4, pp. 1164–1176, Apr. 2012.

[32] D. J. Cecil and E. J. Zipser, "Relationships between tropical cyclone intensity and satellite-based indicators of inner core convection: 85-GHz ice-scattering signature and lightning," *Mon. Wea. Rev.*, vol. 127, no. 1, pp. 103–123, Jan. 1999.

[33] J. Xu and Y. Wang, "Sensitivity of tropical cyclone inner-core size and intensity to the radial distribution of surface entropy flux," *J. Atmos. Sci.*, vol. 67, no. 6, pp. 1831–1852, Jun. 2010.
[34] D. H. Levinson, H. J. Diamond, K. R. Knapp, M. C. Kruk, and E. J. Gibney, "Toward a homogenous global tropical cyclone BT dataset," *Bull. Amer. Meteorol. Soc.*, vol. 91, no. 3, pp. 377–380, Mar. 2010.
[35] G. D. Atkinson, "Investigation of gust factors in tropical cyclones," Joint Typhoon Warning Center, Pearl Harbor, HI, USA, Tech. Note JTWC 74-1, 1974, p. 9.
[36] J.-J. Song, Y. Wang, and L. Wu, "Trend discrepancies among three best track data sets of Western North Pacific tropical cyclones," *J. Geophys. Res.*, vol. 115, no. D12, Jun. 2010, Art. ID. D12128.
[37] K. R. Knapp and M. C. Kruk, "Quantifying interagency differences in tropical cyclone BT wind speed estimates," *Mon. Wea. Rev.*, vol. 138, no. 4, pp. 1459–1473, Apr. 2010.
[38] D. W. Martin, R. A. Kohrs, F. R. Mosher, C. M. Medaglia, and C. Adamo, "Over-ocean validation of the global convective diagnostic," *J. Appl. Meteorol. Climatol.*, vol. 47, no. 2, pp. 525–543, Feb. 2008.
[39] S. A. Ackerman, "Global satellite observations of negative brightness temperature differences between 11 and 6.7 μm," *J. Atmos. Sci.*, vol. 53, no. 19, pp. 2803–2812, Oct. 1996.
[40] A. Lattanzio, P. D. Watts, and Y. Govaerts, "Activity report on physical interpretation of warm water vapour pixels," EUMETSAT, Darmstadt, Germany, Tech. Memo. 14, 2006.
[41] M. T. Montgomery, M. E. Nicholls, T. A. Cram, and A. B. Saunders, "A vortical hot tower route to tropical cyclogenesis," *J. Atmos. Sci.*, vol. 63, no. 1, pp. 355–386, Jan. 2006.
[42] R. A. Houze, M. Bell, and W.-C. Lee, "Convective contribution to the genesis of Hurricane Ophelia (2005)," *Mon. Wea. Rev.*, vol. 137, no. 9, pp. 2778–2800, Sep. 2009.
[43] M. Bister and K. A. Emanuel, "The genesis of Hurricane Guillermo: TEXMEX analysis and a modeling study," *Mon. Wea. Rev.*, vol. 125, no. 10, pp. 2662–2682, Oct. 1997.
[44] T. L. Olander and C. S. Velden, *ADT-Advanced Dvorak Technique Users' Guide (McIDAS Version 8.1.3)*, Madison, WI, USA: University of Wisconsin–Madison, 2011. [Online]. Available: http://tropic.ssec.wisc.edu/misc/adt/guides/ADTV8.1.3_Guide.pdf
[45] P. Ricchiazzi, S. Yang, C. Gautier, and D. Sowle, "SBDART: A research and teaching software tool for plane–parallel radiative transfer in the Earth's atmosphere," *Bull. Amer. Meteorol. Soc.*, vol. 79, no. 10, pp. 2101–2114, Oct. 1998.
[46] I. M. Lensky and D. Rosenfeld, "Satellite-based insights into precipitation formation processes in continental and maritime convective clouds at nighttime," *J. Appl. Meteorol.*, vol. 42, no. 9, pp. 1227–1233, Sep. 2003.
[47] I. M. Lensky and D. Rosenfeld, "A night rain delineation algorithm for infrared satellite data based on microphysical considerations," *J. Appl. Meteorol.*, vol. 42, no. 9, pp. 1218–1226, Sep. 2003.
[48] I. M. Lensky and D. Rosenfeld, "Clouds-Aerosols-Precipitation Satellite Analysis Tool (CAPSAT)," *Atmos. Chem. Phys.*, vol. 8, no. 22, pp. 6739–6753, Nov. 2008.
[49] X.-Y. Zhuge, F. Yu, and Y. Wang, "A new visible albedo normalization method: Quasi-Lambertian surface adjustment," *J. Atmos. Oceanic Technol.*, vol. 29, no. 4, pp. 589–596, Apr. 2012.
[50] K. R. Knapp, "Calibration assessment of ISCCP geostationary infrared observations using HIRS," *J. Atmos. Ocean. Technol.*, vol. 25, no. 2, pp. 183–195, Feb. 2008.
[51] R. A. McClatchey, R. W. Fenn, J. E. A. Selby, F. E. Volz, and J. S. Garing, *Optical Properties of the Atmosphere*, 3rd ed. Tech. Rep. AFCRL-72-0497, Air Force Geophys. Lab., Hanscom AFB, MA, USA, 1972, p. 108.
[52] M. Setvák, D. T. Lindsey, R. M. Rabin, P. K. Wang, and A. Demeterová, "Indication of water vapor transport into the lower stratosphere above midlatitude convective storms: Meteosat second generation satellite observations and radiative transfer model simulations," *Atmos. Res.*, vol. 89, no. 1/2, pp. 170–180, Jul. 2008.

Xiao-Yong Zhuge was born on December 27, 1986. He received the B.S. and Ph.D. degrees in atmospheric science from Nanjing University, Nanjing, China, in 2009 and 2014.

He is currently an Assistant Professor with the School of Atmospheric Sciences, Nanjing University. His current research interests include satellite remote sensing and data assimilation.

Jian Guan received the B.S. degree in atmospheric science from Nanjing University, Nanjing, China, in 2012. He is currently working toward the Ph.D. degree in the Department of Atmospheric and Oceanic Sciences, School of Physics, Peking University, Beijing, China.

His research focuses on paleoclimate changes and model–data comparison.

Fan Yu received the M.S. degree in atmospheric sounding from the Nanjing Institute of Meteorology, Nanjing, China, in 1990 and the Ph.D. degree in meteorology from Nanjing University, Nanjing, in 1998.

Since 1998, he has been with the School of Atmospheric Sciences, Nanjing University, where he is currently a Professor teaching courses on satellite meteorology, atmospheric radiation, and atmospheric sounding. He focuses on research activities in the detection, identification, and retrieval of cloud classification, rainfall rate, 3-D humidity field, land fog and sea fog, etc, by using multispectral satellite information.

Prof. Yu is a Commissioner of the Satellite Meteorology Professional Committee of the Chinese Meteorological Society. He was the recipient of several grants from the National Natural Science Foundation of China.

Yuan Wang received the Ph.D. degree from the Université Catholique de Louvain, Louvain-la-Neuve, Belgium, in 1997.

He is currently a Professor with and the Vice Dean of the School of Atmospheric Sciences, Nanjing University, Nanjing, China. His research fields include synoptic and dynamical meteorology, computational fluid mechanics, design of numerical modeling, and theory of variational assimilation, etc. By April 23, 2015, he has published more than 50 papers in peer-reviewed journals.